



Real-time advanced ultrasonic imaging of assemblies of glass and SiC mirrors of the extremely large telescope

Mathieu Ducouso^{1,2} · Eric Boujon³ · Frédéric Reverdy³ · Souad Bannouf⁴ · Benoit Puel⁴ · Sebastien Lonné⁴ · Alexandra Guggenheim⁵ · Florent Mallet⁵ · Xavier Tonnellier⁶ · Hugo Mercier-Nallet⁶ · Claire Lamour⁶ · Camille Frapoli⁶

Received: 18 July 2024 / Accepted: 13 December 2024

© The Author(s), under exclusive licence to Springer-Verlag London Ltd., part of Springer Nature 2024

Abstract

The Extremely Large Telescope of the European Southern Observatory (ESO) is currently under construction and is expected to become the world's largest optical/near-infrared terrestrial astronomical observatory. Its optical design incorporates five mirrors of varying shapes, sizes, and materials. The primary mirror, with a diameter of 39 m, is perhaps the most remarkable. The fifth mirror (M5), made of SiC, ranks among the largest tip-tilt mirrors globally. Various structural joining techniques, such as bonding and brazing, are applied to these optical components to enable nanometric relative positioning between the assembled parts. This study reviews advanced real-time ultrasonic imaging based on Total Focusing Methods (TFM) for their inspection. For the M1 mirror, TFM is utilized in a tandem configuration for regular industrial use and is also applied once with Rayleigh waves to inspect the surface and subsurface of the M5 mirror.

Highlights

- Real-time non-destructive imaging of structural bonding and brazing is conducted.
- The Total Focusing Method is employed in tandem configuration.
- A Total Focusing Method with a surface wave is applied.
- A method validated for industrial applications is also implemented.

Keywords Nondestructive testing · Phased-array · Total focusing method · Bonding · Brazing

1 Introduction

The Extremely Large Telescope (ELT) aims to advance astrophysical understanding by facilitating detailed studies of planets around other stars, the first galaxies in the Universe, supermassive black holes, and the nature of the Universe's dark sector [1]. Such advancements are made possible by specific optical features of the instrument [2]. First, the primary mirror (M1) measures nearly 40 m in diameter with a maximum form error of a few nm RMS. This level of performance is achievable due to the mirror's structure, which consists of 798 sub-mirrors referred to as 'segments' (but 931 segments are built to allow a continuous turn over for maintenance). These segments are hexagonal, with characteristic dimensions of 1.44 m diagonally and a glass thickness of approximately 50 mm and around 250 kg. The positioning of each segment relative to its immediate

✉ Mathieu Ducouso
mathieu.ducouso@safrangroup.com

¹ Safran Tech, Rue Des Jeunes Bois,
78114 Magny Les Hameaux, France

² Laboratoire PIMM, Arts Et Métiers Sciences Et
Technologies, CNRS, CNAM, HESAM Université, Paris,
France

³ Eddyfi Technologies, 1 Rue Terre Neuve, 91940 Les Ulis,
France

⁴ Extende, 14 Avenue Carnot, 91300 Massy, France

⁵ Mersen Boostec, ZAE Ceram'Innov Pyrénées, 65460 Bazet,
France

⁶ Safran REOSC, Avenue de La Tour Maury,
91280 Saint-Pierre-du-Perray, France

neighbors is nanometric, maintaining a continuous surface across the primary mirror. Since the mirror is subject to external dynamic forces such as wind, temperature variations, and vibrations, control is achieved through active nanopositioning actuators connected to a warping harness at 27 points on the back face of each segment. The warping harnesses are connected to the M1 segments by structural epoxy bondings. A structural bonding is a joined junction between two structures that can transmit stress without compromising structural integrity. This bonding for the ELT must withstand earthquakes, significant daily thermal variations (Atacama Desert), and other factors over a 30-year lifespan. Ultimately, 27×931 structural connections require inspection for the M1 mirror.

Second, the ELT is equipped with kHz adaptive optics from the quaternary mirror (M4). This setup enables the correction of recorded images from atmospheric turbulence and residual vibrations of the telescope itself. The core of the telescope's adaptive optics is achieved by combining M4 and M5 (the fifth mirror). M5 is a flat, elliptical mirror measuring 2.7 by 2.2 m, enabling fast steering (tip-tilt) to stabilize the field of view after M4 deformations. Despite its large dimensions, the M5 mirror must be lightweight and rigid. Therefore, it is constructed from silicon carbide (SiC) with a complex, optimized shape. SiC enables the mirror to achieve high stiffness-to-weight performance and provides an optical surface that can be polished to the required nanometric RMS roughness. Due to the mirror's dimensions, it comprises six segments brazed together. This large-scale brazing is structural and must be high quality, without voids near the optical surface.

The M1 epoxy bonding and M5 brazing are crucial for the ELT's optical performance, and Non-Destructive Testing (NDT) of these assemblies is required to both ensure their structural function and verify the absence of porosities at or near the optical surface level for M5.

It is challenging to certify the good quality of structural bonding in a non-invasive manner (certifying that it can resist up to a predefined strength value). There is no industrial NDT method available for such certification. Although some solutions are emerging, they remain in the laboratory stage [3–9]. An alternative approach to ensure the quality of structural bonding is to monitor all process steps and evaluate the morphology of the bonding layer (thickness and porosity level) after reticulation. For M1, this requires imaging the bonding layer, which is approximately 400- μm thick and embedded between a glass-ceramic material (Zerodur, Schott) of about 50- mm thick and a metallic part made of invar, approximately 20- mm thick (it has a complex shape with an irregular profile and numerous threaded holes). The black color of the adhesive prevents imaging of the layer using optical methods, even though the mirror is transparent in the visible spectrum. Thermography is also not feasible.

Although M1 is transparent in the visible spectrum, laser light can, in theory, deposit energy in the bonding layer to create a local thermal rise, which can be utilized to image the bonding layer. However, the Zerodur material is opaque in the spectral domain necessary for thermography detection, and thermal diffusion in the bonding layer is not detectable [10]. X-ray radiography is also unsuitable, as the bonding layer's thickness is too minimal relative to the structure's thickness, leading to insignificant variations in gray contrast for detection. Ultrasonic imaging appears to be the optimal approach for imaging the bonding layer. This study uses an advanced ultrasonic imaging technique based on phased arrays and the Total Focusing Method (TFM) [11–13].

The TFM is an ultrasonic array technique utilized to synthetically focus on each point of a region of interest. It is considered by some as the "gold standard" in ultrasound imaging [11]. It is currently employed in conventional reflection geometry [11] or self-tandem configuration by a single phased-array probe configuration due to the probe's large aperture [14]. A two-probe configuration has also recently been used in a tandem configuration in transmission for weld inspection [15]. However, the tandem configuration in reflection has not been realized before this work. This configuration allows the inspection of large areas that are otherwise difficult to access.

Similarly, ultrasound inspection of the M5 brazing is also viable. Magnetic methods are inefficient on this material, and dye penetrant inspection is limited to surface-level evaluation. Thermography is challenging due to restricted access for detection (Fig. 15) because of the mirror's complex geometry and large dimensions, which also limit the use of X-ray radiography or computed tomography. In contrast, the ceramic material used for these mirrors is well-suited for ultrasound inspection, as ultrasonic attenuation due to viscoelastic or scattering effects is low in this material [16, 17]. For M5 inspection, ultrasound imaging based on TFM is also employed. The brazing plane, parallel to the surface and the probe's aperture plane, is successfully imaged using a bulk longitudinal wave and a matrix probe. This configuration facilitates the inspection of interface areas and enables the imaging of adhesion deficiencies. In addition, a linear probe was used on a wedge designed at an angle to generate Rayleigh waves. The effectiveness of this method for surface and sub-surface inspection has recently been demonstrated on metallic parts [18, 19], mainly for imaging sub-millimeter defects. This study demonstrates the method's efficiency for brazing inspection on ceramic materials.

This study reviews an advanced ultrasonic inspection method for the industrial inspection of M1 and M5 mirrors. The first section presents the M1 inspection concerning the 931 segments produced. Initially, the structure and bondings are described. Then, ultrasonic inspection of back-face bondings is discussed, followed by a tandem inspection of

the bondings located on the segment edges. Probe sizing and control simulations are conducted using CIVA before experiments. The second section addresses the M5 mirror inspection, which is performed only once. This section represents the previous structure, briefly introducing the M5 mirror and its inspection requirements. In addition, ultrasonic inspection of the structural part of the brazing using a matrix probe and longitudinal waves is introduced. Finally, optical surface inspection using Rayleigh waves and a linear probe is discussed [14].

2 Inspection of M1 mirror

2.1 Presentation of the mirror

The M1 segment is a hexagonal structure approximately 1.4 m in diameter and 50-mm thick. More specifically, the concave structure of the M1 mirror (with a 71-m radius of curvature) causes thickness variations within and between segments, approximately ± 3 mm around the 50 mm baseline. Each segment has a flat bottom hole 20 cm in diameter and 27-mm deep from the mirror’s back face. Figure 1 illustrates the M1 mirror’s back face, showing the bondings of interest identified by arrays. The dotted array represents the back-face bondings: 27 axial supports and three tooling pads. The solid red array indicates the six bondings performed on the segment edge within the central pocket [15, 16]. These bondings are circular and consist of 4 aligned sub-bondings on the same pad.

Bondings connect the mirror to whiffletrees and must possess structural strength. They are achieved using a structural adhesive. The bonding layer’s thickness and diameter are optically monitored during curing, respectively sub-millimetric and several tens of cm. However, potential porosities

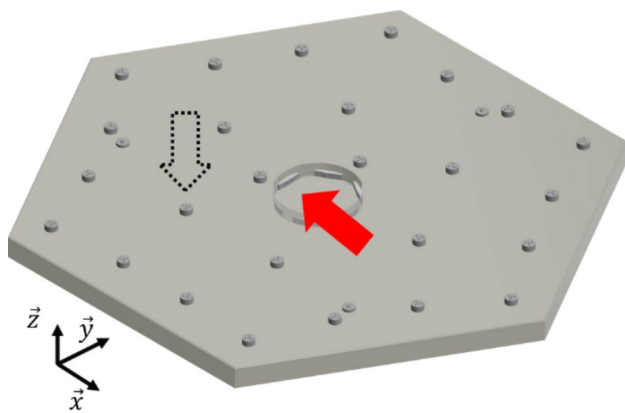


Fig. 1 Representation of the back face of the M1 mirror. Bondings are visible and indicated by a dot vertical array (back face bondings) and a red color arrow (edge bonding)

can go undetected at this stage, necessitating ultrasonic inspection post-curing. Density, longitudinal velocity, and transverse velocity values for Zerodur, glue, and invar, denoted as ρ , V_L , and V_T , respectively, are listed in Table 1 [17].

2.2 Ultrasonic imaging of the back face pads

This evaluation is simple and briefly mentioned in this study to outline the M1 mirror’s comprehensive inspection procedure. Bonding inspection was conducted using a phased array probe in contact (water coupling) with the mirror’s optical face above the bonding, employing a bulk longitudinal wave. Given the bonding layer’s thickness and Zerodur’s relatively low acoustic attenuation, a probe with a 17-MHz central acoustic frequency was utilized. A square matrix phased array probe featuring 11×11 elements (Imasonic, with each element measuring 0.9×0.9 mm and 0.1 mm interspacing), was employed for this inspection.

This probe’s large aperture and high frequency extend the Fresnel zone beyond 50 mm. At normal incidence, the focused beam at 50 mm has a circular shape with a radius of 0.8 mm. However, the probe pitch is greater than the wavelength in Zerodur, resulting in high element directivity. Beam deviation capability was simulated using CIVA software [18] and is illustrated in Fig. 2. The estimated beam deviation ranges from 0 to 25°. An out-of-signal area for normal incidence defines the reference signal. This reference determines the intensity of the focused beam’s acoustic signal and its relation to sidelobes at different incidence angles. The grating lobes, up to 10°, are substantial, leading to energy loss in the focused beam (−7 dB) and increased noise during inspection. This limited beam deviation capability restricts the imaged area within the bonding.

The imaging method is then selected using CIVA software. Initially, the TFM imaging method is considered, with a viewing plane in the bulk of the glue layer and parallel to the active plane of the probe. However, the probe’s limited beam deviation capability restricts the approach’s effectiveness, as the entire bonding cannot be imaged in a single acquisition. In addition, despite the small surface area

Table 1 Elastic properties of the different materials involved in the M1 bondings

Zerodur	ρ (kg/m ³)	2530
	V_L (m/s)	6545
	V_T (m/s)	3740
Glue	ρ (kg/m ³)	1230
	V_L (m/s)	2490
	V_T (m/s)	1135
Invar	ρ (kg/m ³)	8100
	V_L (m/s)	4830
	V_T (m/s)	2620

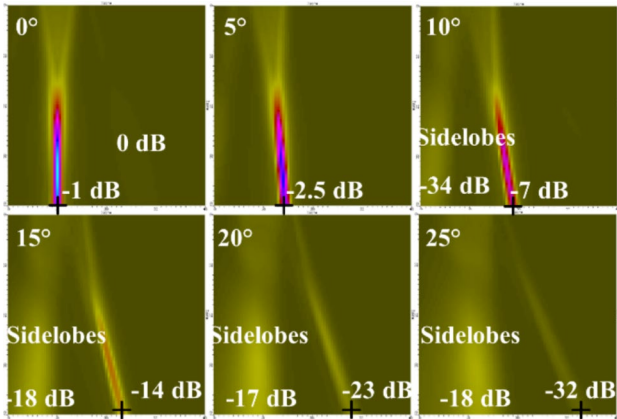


Fig. 2 Ultrasound beam deflection capability in that inspection case simulated using CIVA software. Images color are in the dB scale

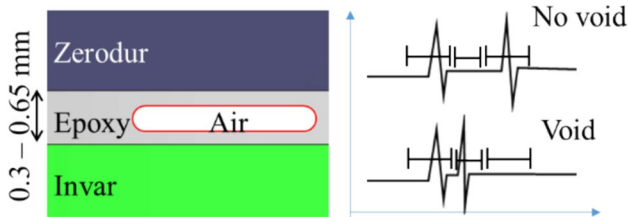


Fig. 3 Left side represents the simulated bonding, including a void of air. The right side depicts the detected signal and the gates that generate images. Almost all the signal is reflected on the epoxy/air interface in the presence of a void

that can be imaged, the thickness variations of the Zerodur require imaging a large volume (a few millimeters in thickness), resulting in acquisitions exceeding 1.5 GB per bonding.

A 3D-sector scan is used instead of TFM. Applied delay laws allow the beam to focus along a few millimeter line in the bulk of the bonding layer. A 2D manual encoder is utilized to generate images. Ultrasonic images of the bonding layer are then obtained by synchronizing the reflected signal from the Zerodur/glue interface of one acquisition gate on the reflected signal from the back face of the bonding layer and one acquisition gate between the two reflected signals, as illustrated in Fig. 3. This approach requires only a single acquisition file for all the bondings, which occupies only a few MB. Figure 4 depicts an example of an image obtained using this approach. It compares two images: an ultrasonic testing image (left) and an X-ray computed tomography image (right, with a voxel size of 40 μm). These images are captured from a reference bonding employed to calibrate the NDT procedure. The black quasi-circles in the gray area of the X-ray image correspond to porosities in the bonding layer. Porosities larger than 1 mm in diameter are well identified in the ultrasonic image, which is required for that

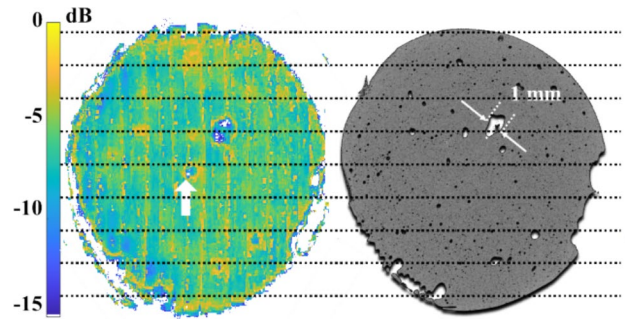


Fig. 4 Comparison between an ultrasonic inspection (left, dB scale) and an image obtained from computed X-ray tomography of a representative bonding of the back face of the M1 mirror of ELT. Images are at the same scale. Dotted lines are placed to help make a comparison between images

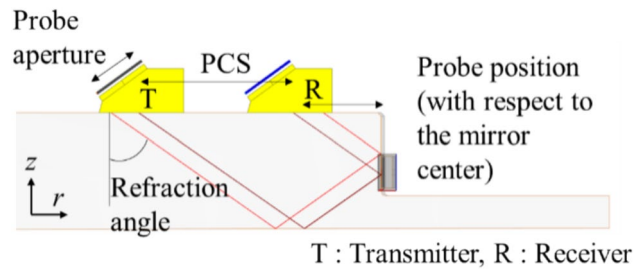


Fig. 5 Scheme of the tandem inspection of the edge bonding simulated using CIVA

inspection. In addition, an extra indication is detected at the center of the bonding on the ultrasonic image (indicated by a vertical arrow), which is absent in the X-ray image. This indication corresponds to a hole in the invar pad, which is utilized to inject the epoxy bonding with a syringe.

2.3 TFM imaging of the edge bonding using a tandem configuration

The distance between the external edge of the mirror and the bondings in the central pocket appears too long, especially at high frequency, to inspect using a similar approach. In addition, the hexagonal shape of the mirror complicates focusing the beam in the bonding layer, as the central pocket is cylindrical. Therefore, a tandem approach using linear PA probes and TFM imaging is chosen to inspect the bondings. Scheme of tandem experiment from CIVA software is represented on Fig. 5. A cylindrical manual scan, co-centered with the mirror, allows imaging of the bondings. Initially, simulations are performed using CIVA to validate the tandem approach and to determine the experimental apparatus. The inspection frequency is examined in simulations ranging from 10 to 20 MHz. Echoes from the front and back faces of the bonding

are well differentiated at 15 MHz in shear propagation. This frequency is chosen as ultrasonic attenuation increases with the square of the frequency.

Once the inspection frequency is defined, the refraction angle, probe aperture, probe position (relative to the central pocket border), and Probe Center Spacing (PCS) are optimized. The phased array acquisition system, a 128-channel driver, allows each probe to have a maximum of 64 elements. The probe aperture is linked to the pitch and defined for the wavelength in Zerodur. A parametric study involving four variables is conducted to identify the optimal configuration. A flowchart of the methodology utilized to find the optimal experimental configuration is shown in Fig. 6. Initial simulations are performed in 2D to reduce calculation time, thus not accounting for the cylindrical nature of the control at this stage. A final 3D simulation is then conducted to validate the configuration for the mirror setup, as illustrated in Fig. 9. The optimal configuration enables a clear visualization of the simulated voids in the glue layer (high signal dynamic) and provides a consistent signal dynamic independent of the z-position of the voids in the bonding layer. Three voids of 1.5-mm diameter are simulated in the bonding layer, evenly distributed along the z-axis.

The refraction angle enables tuning the amplitude of the reflected wave from the Zerodur/epoxy interface compared

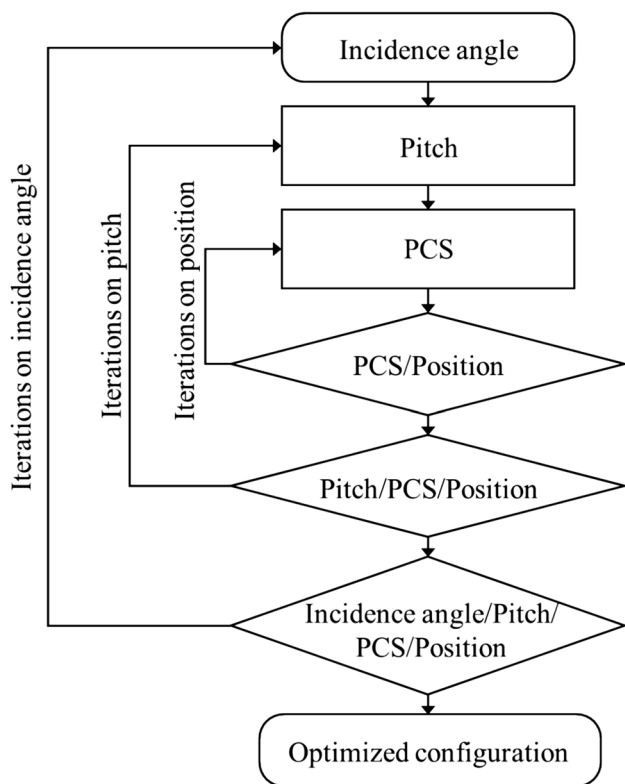


Fig. 6 Flowchart of the simulations to find the optimal experimental configuration for tandem inspection of edge bonding in M1

to the epoxy/invar interface. For instance, with a refraction angle of 45°, the first echo from the Zerodur/epoxy interface is much stronger than the second echo from epoxy/invar (which is of low amplitude). At 55°, the two echoes exhibit similar amplitudes. This configuration improves detection beyond the Zerodur/epoxy interface by reducing the amplitude of the first interface echo. However, further increasing the refraction angle induces variations in the signal amplitude along the z-axis, as shown in Fig. 7. The simulated detected signal from three aligned voids at different z-positions is presented in Fig. 7. Increasing the angle amplifies the signal amplitude from the voids and do not allow to generate a homogeneous image as function of z during the imaging procedure. However, this amplitude remains inconsistent until reaching 55°. Thus, the optimal refraction angle is considered to be 55°.

The optimal PCS and probe positions vary non-monotonically with pitch. The analysis uses analysis similar to those shown in Fig. 7. The optimal probe position and PCS are determined for each pitch value. A pitch equal to three times the wavelength is identified as the optimal configuration, considering both signal dynamics and amplitude homogeneity along the z-axis.

Beam focalization in the passive plane of the probes is considered. Three configurations are analyzed: no focalization, identical focalization, and optimal focalization for each probe. In each configuration, the optimal probe is identified. Without focalization, the optimal probe design is determined for an elevation of 7.5 mm. The beam size is calculated from the convolution between the emission and reception beams

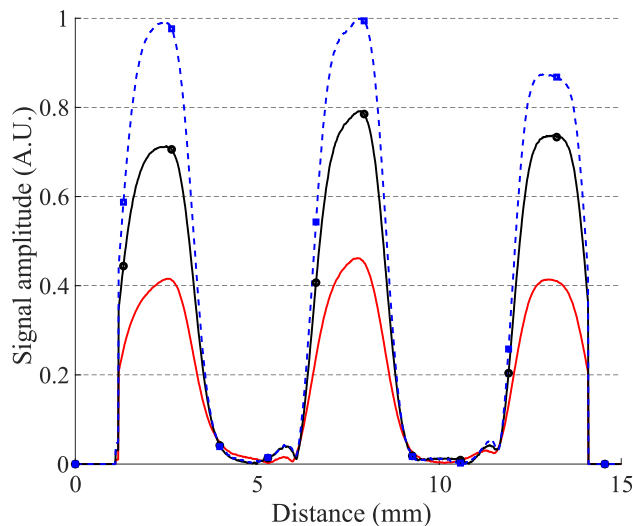


Fig. 7 Amplitude of the signal extracted from the TFM image of void detection in the bonding layer depending on the refraction angle. Curve without symbol:refraction angle of 45°; Continuous line with symbol:refraction angle of 55°; Dotted line with symbol:refraction angle of 60

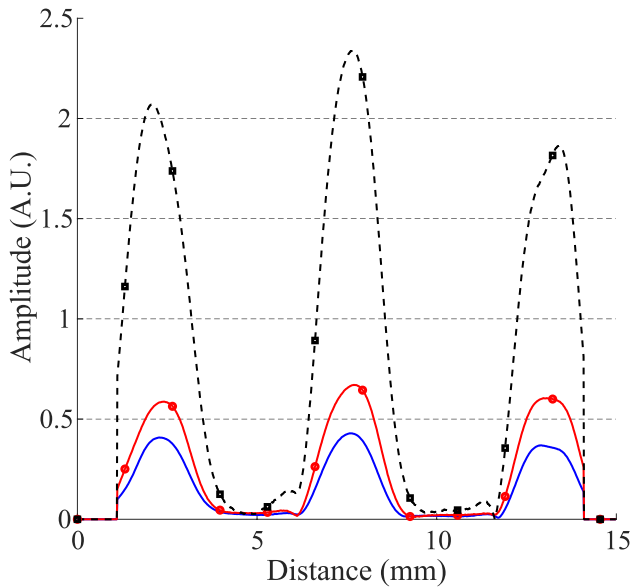


Fig. 8 Amplitude of the signal extracted from the TFM image of void detection in the bonding layer depending on the passive focalization. Curve without symbol: no focusing; Continuous line with symbol: identical focusing; Dotted line with symbol: optimal focusing for each phased-array

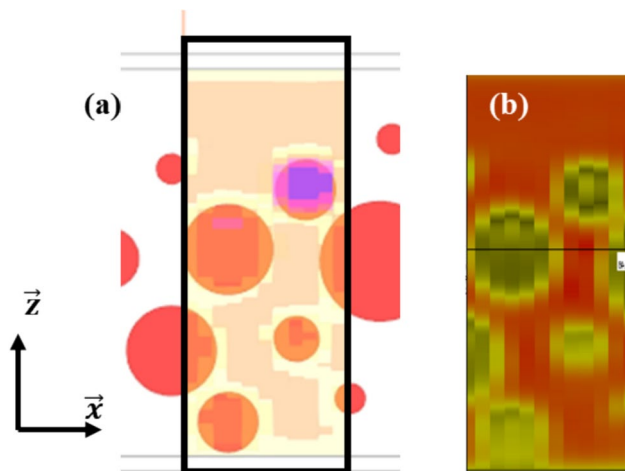


Fig. 9 Simulation of the inspection of the edge bondings. (a) CAD of the scanning zone. The simulated inspected area is in the rectangle. Red circles represent voids in the glue layer. Ultrasonic image along \vec{x} axis is obtained from mechanical displacement and image along the \vec{z} axis is obtained from TFM imaging. (b) Simulated inspection using CIVA software from optimized configuration

and is evaluated at $0.8 \times 4 \text{ mm}^2$. Considering identical focalization in the passive plane for both probes, the optimal configuration achieves an elevation of 17 mm and a curvature radius of 100 mm. The focused beam is measured at $0.8 \times 1.4 \text{ mm}^2$. Finally, the optimal configuration is determined for

two different radii for the transmitter and receiver, reflecting the different acoustic paths at 250 and 100 mm, respectively. The focused beam is also measured at $0.8 \times 1.4 \text{ mm}^2$, but the correlation image of the focused beam shows lower noise in the outer zone of the beam compared to using the same radius for both probes. The signal amplitude strongly correlates with elevation, but an elevation of 20 mm is the upper limit for manufacturing.

Figure 8 highlights the importance of focusing the beam in the passive plane. It presents the amplitude of the signal extracted from the TFM image of voids in the bonding layer, considering the optimally identified configurations. The configurations considered include no focusing (blue continuous curve without symbol), identical focusing (red continuous curve with symbol), and different focusing (black dotted curve with symbol) for the two probes in the passive plane. The signal amplitude as a function of z is almost similar for all the optimized configurations, which is a primary requirement. In addition, using similar focusing for both probes does not significantly improve the amplitude of the void signal. This lack of improvement occurs because, in this scenario, the focus is optimized for detection but not for emission. Hence, the incoming signal is far from the focus and relatively low in amplitude. In this scenario, the beam is spatially large in the passive plane, which substantially limits the lateral resolution during manual inspection. Finally, the optimal configuration significantly improves the signal on the TFM image from voids, and the beam size, $0.8 \times 1.4 \text{ mm}^2$, allows imaging the bonding with sufficiently high spatial resolution.

Simulations of the inspection are performed, considering bonding that presented voids with diameters ranging from 1 to 5 mm, as illustrated in Fig. 9. Simulations with mechanical scanning demonstrate that it is possible to obtain an image of the entire surface of the defect. Sizing at -6 dB provides accurate results, considering the error linked to the scanning step and the TFM grid. When multiple defects at varying depths are present in the glue joint, the TFM image of the background can detect their presence due to the shading effect they produce. Thus, the image of the bottom of the glue joint is a reliable indicator of defect presence.

This analysis enables the design of the required configuration for inspection. Particular attention must be directed to the centripetal alignment of the probes. Since the path lengths in transmission and reception are approximately 160 and 55 mm, respectively, and the beam focus is on a millimeter scale, the angular positioning accuracy relative to the normal of the disk must be less than 0.5° to achieve half-covering of the focal transmission and reception beam spots.

Initial demonstration were conducted on a monolithic aluminum sample with thickness and elastic properties similar to those of Zerodur. A 3-mm diameter and depth

Flat Bottom Hole (FBH) was inserted at the sample’s mid-thickness. TFM imaging of the FBH can be achieved using either Full Matrix Capture (FMC) or Plane Wave sequences. However, the best SNR was obtained with Plane Wave Imaging (PWI). The Region of Interest (ROI) measures $50 \times 5 \text{ mm}^2$, with a 0.05-mm pixel size. Imaging was conducted in real-time at a frequency of 30 Hz. Experimental results are illustrated in Fig. 10, where the FBH is imaged in the three spatial planes. In the horizontal plane, only the bottom of the hole is visible.

Finally, M1 bondings were inspected. This inspection is more challenging than the FBH, as the probing wave must exit and re-enter the glass mirror. Therefore, the gain is increased by 10 dB. Figure 11 presents an image of the bondings. Four sub-bondings are visible in this image. The first three sub-bondings (labeled 1 to 3 in Fig. 11) on the left show no indications, whereas two voids, opposed and marked by arrows in Fig. 11, were detected in the sub-bonding labeled 4. After peeling, these were identified as voids with millimeter diameters, showing good spatial correspondence with the ultrasonic image Fig. 11.

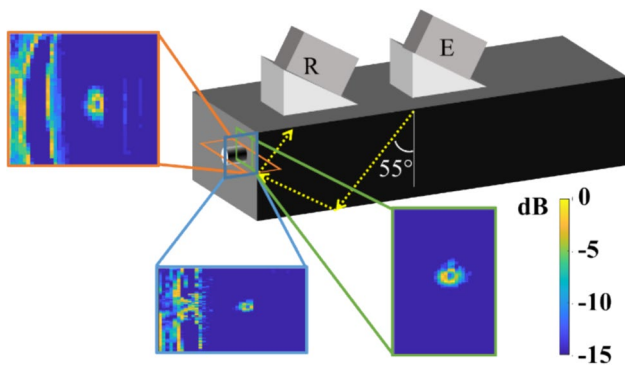
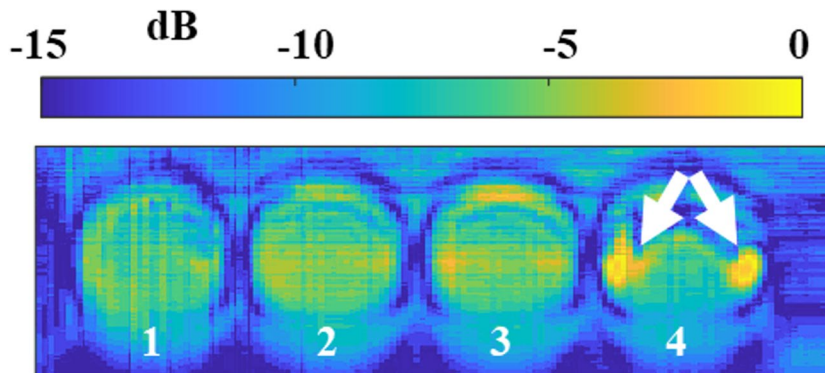


Fig. 10 Illustration of the imaging using the Total Focusing Method of an FBH in a monolithic aluminum sample using a tandem approach. Images are in the dB scale

Fig. 11 Ultrasonic image of the bondings performed on the edge of the segment. The image was obtained using the tandem configuration presented with a PWI visualization. Sub-bondings 1 to 3 do not show defects while sub-bonding 4 presents 2 voids opposed. The image color is in the dB scale



3 Inspection of the M5 mirror

3.1 Presentation of the mirror

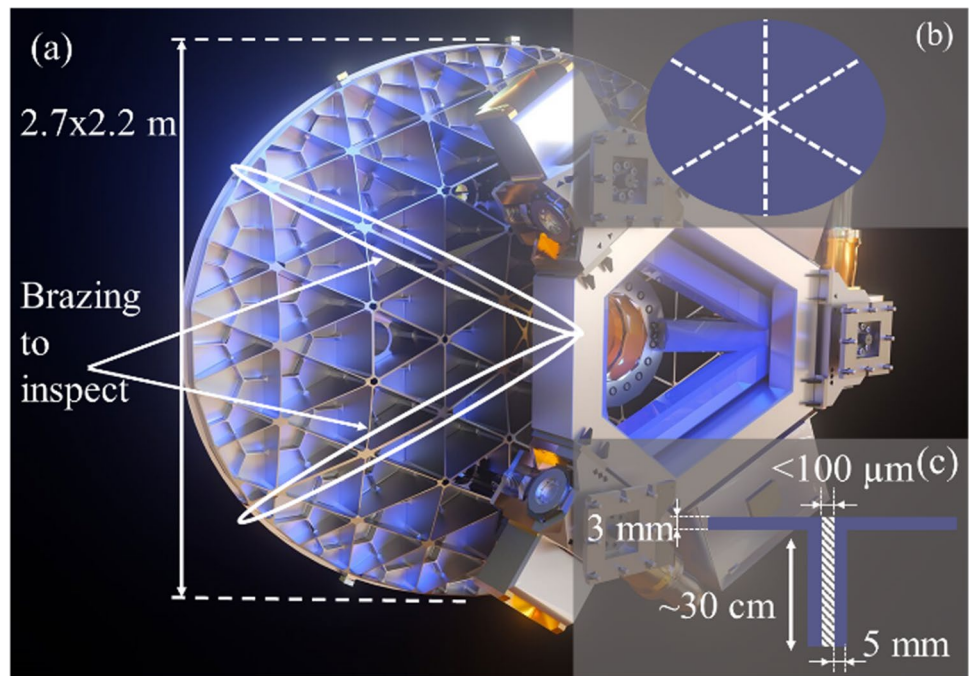
M5 is a flat, elliptical mirror measuring $2.7 \times 2.2 \text{ m}$. It is constructed from six lightweight silicon-carbide (SiC) segments, formed by sintering and then brazed together to create the monolithic mirror. This material is selected for its exceptional structural properties. Its density (ρ) and Young’s (E) and shear (μ) moduli are provided in Table 2 [19]. The moduli values remain constant across temperatures from -200 to $+1000 \text{ }^\circ\text{C}$. This material is not only highly rigid but also extremely light. These properties, along with a specific and optimal morphological shape, facilitate the design of a rigid, lightweight mirror that enables the fast tip-tilt optical system. In addition, these properties significantly influence ultrasonic inspection, as bulk longitudinal and transverse waves propagate at exceptional velocities of approximately $12,000 \text{ m/s}$ and 7500 m/s , respectively. At 15 MHz , these velocities correspond to 0.8 mm and 0.5 mm wavelengths about two orders of magnitude larger than the SiC microstructure [20], resulting in no detectable scattering.

Segment sintering and brazing are performed by Mersen Boostec (France) [21]. The thickness of the brazing is less than $100 \text{ }\mu\text{m}$. The very low attenuation observed during the evaluation reflects the quality of the manufactured material [22]. An artist’s view of the ELT M5 mirror is shown in Fig. 12a. Figure 10b depicts the mirror’s optical face, symbolizing brazing with dotted lines. Figure 10c illustrates a sectional view of the thickness of the mirror.

After assembly, an inspection of the brazing must be conducted. Two different inspections are performed for two

ρ (kg/m^3)	3210
E (GPa)	420
μ (GPa)	180

Fig. 12 Artiste view of the ELT M5 mirror. The mirror is connected to the tip-tilt system. Such a view allows an understanding of the complex shape to optimize the ratio rigidity/weight. Source from ESO. (ELT M5 mirror (artist's impression) | ESO). Insert **b** illustrates the brazing (white dot lines) of the different parts of the mirror. Insert **c** depicts the characteristic dimensions of interest



different purposes. First, a control is achieved to guarantee the structural properties of the mirror. The mirror should behave as a monolithic structure during the fast tip-tilt solicitations. This is only possible if the brazing is homogeneous throughout the approximately 30-cm height of the structure. Second, before the polishing process, which must allow the mirror to have a nanometric roughness, surface and subsurface inspections are necessary to ensure the absence of porosity in the brazing within a skin depth of slightly less than $100 \mu\text{m}$. The descriptions of these two inspections are presented.

3.2 Inspection of the structural brazing

This inspection focuses on the brazing conducted within the thickness of the mirror, between its various elementary parts. It searches for any deficiencies in the brazing. Large-scale deficiencies are prohibited, and small-scale ones must be identified and measured to assess their potential harmfulness and impact on tip-tilt movements. Given the mirror's dimensions and complexity, a contact inspection using water coupling was performed. Due to the complexity of the mirror's back face (Fig. 12a), employing a simple probe and 2D spatial encoder proved impractical; therefore, advanced ultrasonic imaging was utilized instead.

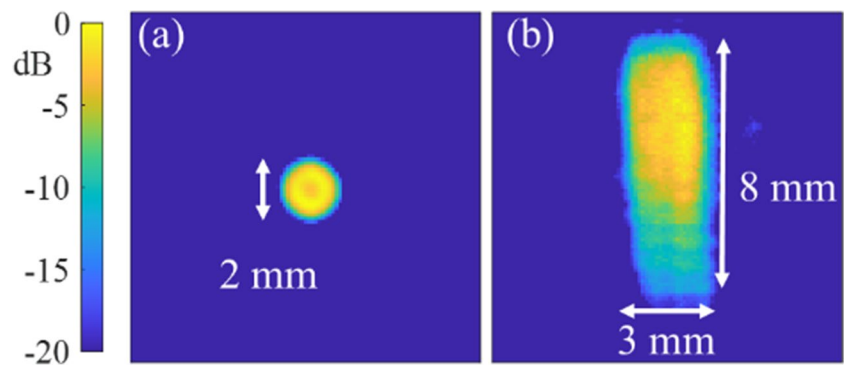
The same matrix phased array probe was employed to inspect the back face pads of the M1 mirror. In that scenario, the constant thickness of the SiC layer before brazing facilitated the use of TFM imaging, which utilizes a visualization plane parallel to the active plane of the probe and within the brazing layer. The ROI measures $10 \times 10 \text{ mm}^2$ with a pixel

size of 0.05 mm^2 . Imaging is conducted in real-time, and if a lack of brazing is detected, an image and the probe position are recorded. The method's performance is demonstrated on a reference block that includes an FBH with a 2-mm diameter (Fig. 13a). The inspection of M5 reveals a small number of brazing deficiencies. Figure 13b is an illustration of one such deficiency.

3.3 Inspection of the mirror face

Once the structural brazing is certified, an inspection of the optical face must be conducted prior to its polishing. This operation is time-consuming due to the ceramic nature of the material and poses challenges because surface or subsurface voids can generate cracks through stress relaxation during the process. Therefore, a surface inspection is required before commencing the operation. Detecting voids in a subsurface skin depth of approximately 1 mm is desired. Dye penetrant inspection is effective for detecting emerging cracks but fails to identify defects beneath the surface. In addition to dye-penetrant inspection, Rayleigh waves were employed [14, 23]. These propagate at the material's surface with a displacement field in a skin depth close to the wavelength and have recently been utilized for real-time inspection of surface and subsurface defects in metallic materials [14, 23]. Complex displacement fields featuring longitudinal and transverse polarization in the plane normal to the surface make Rayleigh waves sensitive to minimal variations in material properties, such as segregations in metallic parts. In addition, their relatively low velocity compared to bulk waves enables the detection of minimal defects, as small as

Fig. 13 TFM imaging of a reference FBH of 2 mm diameter **a** and a lack of brazing detected on the M5 mirror. Image color are in the dB scale



100 μm in characteristic size, at 15 MHz [23]. The estimated Rayleigh wave velocity in SiC is 6700 m/s. Figure 14 the corresponding wavelengths are approximately 0.45 mm at 15 MHz and 0.8 mm at 8 MHz, about half the longitudinal wavelengths at the same frequencies. Accordingly, using Rayleigh waves presents at least two advantages over longitudinal waves: first, at a given frequency, the achievable resolution, proportional to the wavelength, is approximately twice as good using Rayleigh waves as opposed to longitudinal waves. Second, surface inspection using Rayleigh waves is intrinsically simpler, as the waves propagate in this area, whereas subsurface inspection using bulk waves is known to be challenging, even with TFM imaging [24].

Thus, voids under the surface of a few tens of microns can be detected using this approach. The detailed principle is presented in the literature [14], and a schematic representation of the experiments is presented in Fig. 10. The PA probe is parallel to the brazing and is fixed to a wedge at an angle corresponding to the critical Rayleigh wave angle for the rexolite/SiC interface. In this way, Rayleigh waves are generated at the material's surface. The ROI is positioned in front of the wedge, on each side of the brazing, illustrated by the grid on the mirror's surface. Then, classical Total Focusing Methods are used to compute the Rayleigh wave velocity for the TFM summation. An 8 (15) MHz PA probe

(Imasonic, France), composed of $N=128$ elements, with a pitch of 0.25 (0.15) mm and dimensions along the passive plane of 8 (5) mm, was used for inspection. The lower the frequency, the thicker the inspection. The bandwidth at -6 dB is 75 (70)%. The optimal imaging procedure was identified using a Plane Wave Imaging sequence with a classical algorithm for summation. Initial tests were performed on a scale 1 model of the mirror Fig. 15. A few indications were detected under the surface (not detectable using penetrant testing nor optical microscopy observation) and are currently being investigated.

4 Conclusion

This study presents some ultrasonic NDT developments performed for ELT optical mirrors. The developments rely on the mirror for production and daily use inspection (M1) or one-time expertise (M5). However, the common point of such developments is the use of phased-array devices and state-of-the-art ultrasonic imaging methods for NDT. A TFM imaging approach using a tandem approach in reflection is developed for the M1 mirror. It allows sub-millimetric resolution despite an acoustic travel path of several tens of cm. This is the first time such a configuration has been done

Fig. 14 Illustration of the surface inspection of the M5 optical mirror using Rayleigh waves. The ROI from either side of the brazing. The ROI size is $38 \times 30 \text{ mm}^2$ with a 0.03 (0.03 mm² pixel size)

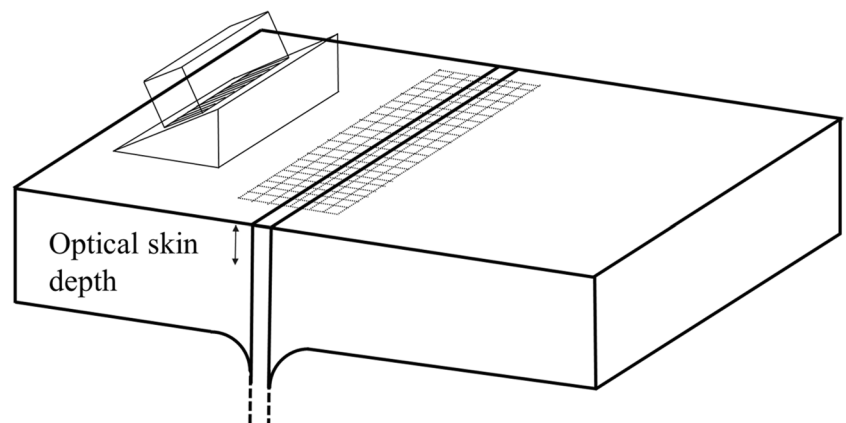
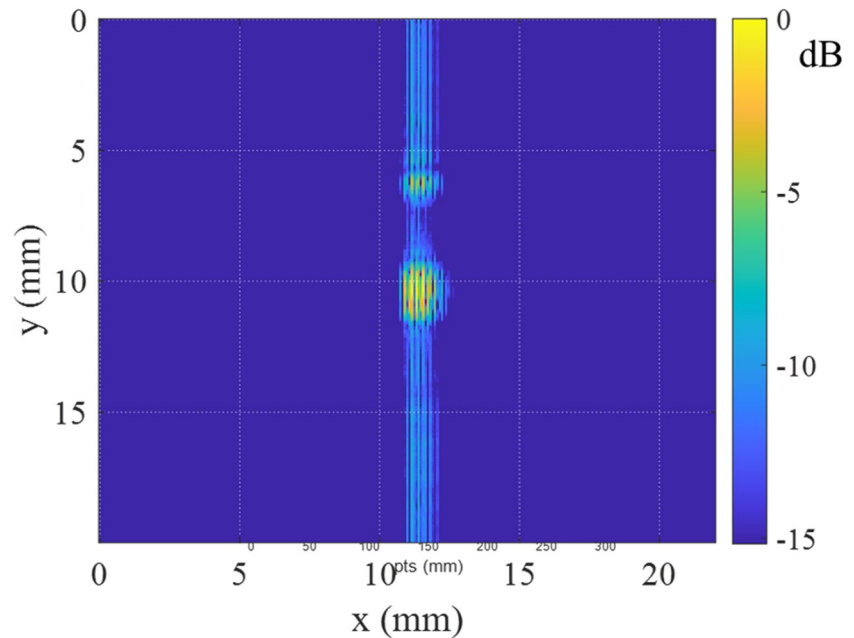


Fig. 15 Ultrasonic image of surface inspection of scale 1 model of the mirror. Indications are detected in a sub-surface skin depth in the brazing. The image color is in the dB scale



with TFM imaging. This work generally opens up prospects for complex access inspections, such as brazing inspections on nuclear power plants for instance. The interest in ultrasonic phased-array inspection for the space industry to guarantee bonding quality is demonstrated. Since this initial work, several similar inspections have been performed on satellite and telescope mirrors. For the M5 mirror, a real-time surface inspection method based on ultrasonic synthetic imaging using Rayleigh waves is used. This method is applied to inspect the surface and sub-surface of the mirror. This modern surface inspection method is applied for the first time in industrial inspection. The frequency is planned to be increased to around 20 MHz to improve the inspection resolutions. Structural health monitoring solutions are also in development for in-service real-time inspections of telescope mirrors.

Author contribution M. D. conceptualized the controls and performed the first experiments and the manuscript writing. E. B. and F. R. realized controls with M. D. and S. B.; B. P. and S. L. realized the simulations. A. G. and F. M. were responsible for developing the M5 mirror at Mersen. X. T. H. M.-N., C. L., and C. F. were responsible for developing the mirrors at Safran REOSC. All the authors read and corrected the manuscript.

Declarations

Competing interests The authors declare no competing interests.

References

1. The Extremely Large Telescope The World's Biggest Eye on the Sky; <https://elt.eso.org/>
2. Gilmozzi R, Spyromilio J (2007) The European extremely large telescope (E-ELT). *Messenger* 127:11–19
3. Ducouso M, Bardy S, Rouchausse Y, Bergara T, Jenson F, Berthe L, Videau L, Cuvillier N (2018) Quantitative evaluation of the mechanical strength of titanium/composite bonding using laser-generated shock waves. *Appl Phys Lett* 112:111904
4. Hodé R, Raetz S, Blondeau J, Chigarev N, Cuvillier N, Tournat V, Ducouso M (2020) Nondestructive evaluation of structural adhesive bonding using the attenuation of zero-group-velocity Lamb modes. *Appl Phys Lett* 116:104101
5. Hodé R, Raetz S, Chigarev N, Blondeau J, Cuvillier N, Gusev V, Ducouso M, Tournat V (2021) Laser ultrasonics in a multilayer structure: plane wave synthesis and inverse problem for nondestructive evaluation of adhesive bondings. *J Acoust Soc Am* 150:2076
6. Zabbal P, Ribay G, Jumel J (2021) Evaluation of metallic bonded plates with nonlinear ultrasound and comparison with destructive testing. *NDT E Int* 123:102514
7. Tighe R, Dulieu-Barton J, Quinn S (2016) Identification of kissing defects in adhesive bonds using infrared thermography. *Int J Adhes Adhes* 64:168–178
8. Shin PH, Webb SC, Peters KJ (2016) Pulsed phase thermography imaging of fatigue-loaded composite adhesively bonded joints. *Ndt E Int* 79:7–16
9. Dumont V, Badulescu C, Stamoulis G, Adrien J, Maire E, Lefèvre A, Thévenet D (2020) On the influence of mechanical loadings on the porosities of structural epoxy adhesives joints by means of in-situ X-ray microtomography. *Int J Adhes Adhes* 99:102568
10. S Industry. "TIE-43: Optical properties of ZERODUR - Technical Information. https://lightmachinery.com/media/1554/tie-43_optical_properties_of_zerodur.pdf

11. Drinkwater BW, Wilcox PD (2006) Ultrasonic arrays for non-destructive evaluation: a review. *NDT E Int* 39:525–541
12. Holmes C, Drinkwater BW, Wilcox PD (2005) Post-processing of the full matrix of ultrasonic transmit–receive array data for non-destructive evaluation. *NDT E Int* 38:701–711
13. Le Jeune L, Robert S, Lopez Villaverde E, Prada C (2016) Plane Wave Imaging for ultrasonic non-destructive testing: generalization to multimodal imaging. *Ultrasonics* 64:128–138
14. Ducouso M, Reverdy FF (2020) Real-time imaging of microcracks on metallic surface using total focusing method and plane wave imaging with Rayleigh waves. *NDT E Int* 116:102311
15. Frapolli C, Bardon D, Ferachoglou N, Chaussat G, Haret LD, Hatzigeorgopoulos J, Armougom J, Pron M, Lesongeur P, Boillet F, Bourgois R, Denis A, Julienne S, Gouedard M, Förster A, Cayrel M (2022) Key challenges for the production of ELT M1 segments at SAFRAN Reosc Society of Photo-Optical Instrumentation Engineers (SPIE) Conference Series 12188
16. Frapolli C, Couteret C, Bardon D, Delfosse A, Chaussat G, Bacouel A, Lesongeur P, Boillet F, Denis A, Julienne S, Gouedard M (2023) Year one into ELT M1 segments manufacturing. *Proc SPIE* 12778:127780A
17. Gerlich D, Wolf M (1978) Thermoelastic properties of Zerodur® glass-ceramic. *J Non-Crystal Solids* 27:209–214
18. Extende CIVA 2023 : Release Note; available on Extende website : https://www.extende.com/files/extende/download_files/CIVA_2023_Release_Note_EN.pdf
19. Donahue CM, Remillieux MC, Singh G, Ulrich TJ, Migliori RJ, Saleh TA (2019) Measuring the elastic tensor of a monolithic SiC hollow cylinder with resonant ultrasound spectroscopy. *NDT E Int* 101:29–33
20. Hayun S, Paris V, Mitrani R, Kalabukhov S, Dariel MP, Zaretsky E, Frage N (2012) Microstructure and mechanical properties of silicon carbide processed by Spark Plasma Sintering (SPS). *Ceram Int* 38:6335–6340
21. Mercier Ythier R, Harel E, Bardon D, Couteret C, Meunier R, Lamour C, Cayrel M, Haupt C, Araujo Hauck C, Muller M 2022 ELT mirrors (M2, M3, M4, M5) production status at SAFRAN Reosc. *Proc SPIE* 12188
22. Baaklini GY, Generazio ER, Kiser JD (1987) High frequency ultrasonic characterization of sintered SiC. 11th Annual Conference on Composite and Advanced Ceramic Materials
23. Ducouso M, Ghibaud O, Amiel S (2024) Surface imaging using total focusing method on surface waves for nondestructive testing. *NDT E International* 146:103176
24. Couret L, Paul N (2022) Lighting the blind zone of ultrasonic phased array probe. Conference: BINDT

Publisher's note Springer Nature remains neutral with regard to jurisdictional claims in published maps and institutional affiliations.

Springer Nature or its licensor (e.g. a society or other partner) holds exclusive rights to this article under a publishing agreement with the author(s) or other rightsholder(s); author self-archiving of the accepted manuscript version of this article is solely governed by the terms of such publishing agreement and applicable law.